Chapter 2
High-Speed InP-Based Long-Wavelength VCSELs

Silvia Spiga and Markus C. Amann

Abstract The rapid growth of internet and cloud computing applications drives a huge demand for bandwidth capacity in communication networks, while power consumption, cost, and space density must scale down. This growth leads to an increase in the size of data centers (longer optical links), and of the fibers' channel data rate, rooted in Moore's Law. Until now, multi-mode fibers (MMF) have been largely employed in datacom applications due to the large coupling tolerance. However, the data-carrying capability of MMF decreases with the transmission distance due to pulse broadening resulting from modal and chromatic dispersion. In order to overcome those limits, transceivers based on single mode fiber (SMF) are under development and the first systems are on the market. Vertical-cavity surface-emitting lasers (VCSELs) are the transmitters of choice for short-reach applications due to their low cost, energy efficiency, and small footprint. InP-based VCSELs emitting at long wavelengths (i.e. 1.3 and 1.55 μm) have gained large interest due to their intrinsic lower power consumption (lower band gap) and low losses in silicon waveguides and silica-based optical fibers, which allows longer transmission distances. While short-wavelength GaAs-based VCSELs have achieved small-signal modulation bandwidths up to 30 GHz [1], InP-based VCSELs show inferior modulation capabilities [2, 3]. Up to date, the highest small-signal bandwidth demonstrated on InP-based devices is 22 GHz [3]. The distributed Bragg reflectors (DBRs) commonly used for GaAs-based VCSELs are made of binary and ternary semiconductor compounds, which offer several advantages such as high refractive-index contrast between the layers, good electrical conductivity and low thermal resistivity. The inferiority of semiconductor DBRs lattice matched to InP challenges the modulation bandwidth enhancement of InP-based devices which suffer of poor thermal conductivity, and high lateral spreading resistance. A further challenge is the single-mode laser operation that has motivated the transition from MMF to SMF in datacom systems. In this chapter, the

S. Spiga · M.C. Amann (✉)
Walter Schottky Institut, Technische Universität München, Munich, Germany
e-mail: amann@wsi.tum.de

S. Spiga
e-mail: Silvia.Spiga@wsi.tum.de

G. Eisenstein and D. Bimberg (eds.), *Green Photonics and Electronics*,
NanoScience and Technology, DOI 10.1007/978-3-319-67002-7_2

challenges related to InP-based VCSELs are discussed with focus on active region design, cavity engineering, and current and optical confinement. These arguments apply to all InP-based VCSELs with emission wavelength between 1.3 and 2.0 μm. Stationary and dynamic characteristics are presented for a 1.55 μm VCSEL. Finally, datacom and telecom transmission experiments are presented.

2.1 InP-Based VCSELs

The absorption spectrum of silica-based optical fibers presents two main windows for datacom and telecom with low absorption around 1.3 and 1.55 μm. GaAs-based VCSELs shows excellent stationary and dynamic performances on the short wavelength regime (i.e. 850 and 980 nm) and take full advantage of their well-established technology. Wavelengths up to 1.3 μm have been achieved for GaAs-based VCSELs by means of highly strained GaInAs quantum wells (QWs) [4], GaInNAs QWs [5], and InAs-GaInAs quantum dots [6]. InP-based VCSELs offer, on the other hand, the advantage of growing quantum wells consisting of moderately (compressively) strained quaternary-materials such as AlGaInAs and InGaAsP emitting at wavelengths between 1.3 and 2.0 μm fully covering the optical fibers low-loss windows.

The key rules for designing a high-speed energy-efficient VCSEL are well known. First, the laser active region has to be able of properly confining the carrier and providing high differential gain. Second, the laser's cavity has to be as short as possible to reduce the photon lifetime boosting the laser relaxation resonance frequency and decreasing the intrinsic damping. Finally, current and optical field have to be properly confined. This allows electrical excitation of the optical mode that contributes to carry the transmitted information, and in guiding the relative longitudinal mode in the laser's cavity such that optical losses are minimal.

The active region composition, the cavity design concepts as wells as electrical and optical confinement to achieve high-speed energy-efficient InP-based VCSELs will be discussed in this section.

2.1.1 Active Region

The design of the active region plays a crucial role for stationary and dynamic performances of VCSELs. Different material systems have been proposed and demonstrated. QWs are used in VCSELs to produce a 2-D density of state (DOS) [7], and to allow high strain (ε) [8]. The step-like DOS of QWs enhances the differential gain. The strain reduces the valence-band DOS enabling population inversion to be reached with smaller carrier concentration, and has the effect of decreasing linewidth, chirp and the threshold current, and increasing slope efficiency, output power, and differential gain [9].

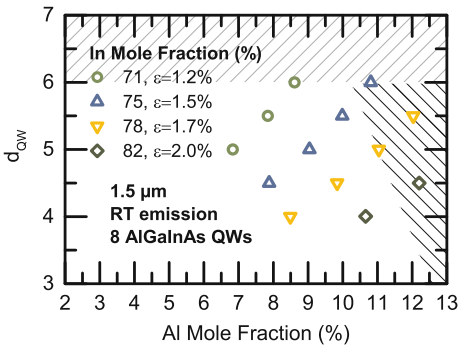

Fig. 2.1 Required QW thickness versus Aluminium mole fraction in the $Al_xGa_yIn_{1-x-y}As$ material system with 7-nm thick $Al_{0.274}Ga_{0.203}In_{0.523}As$ barriers in an active region designed for 1.5 µm emission at room temperature. The shaded area is not accesible for an active region with 8 QWs (see text)

QWs based on quaternary materials offer the advantage of freely designing the emission wavelength and the strain. For the quaternary material system AlGaInAs, Aluminum is used to increase the energy gap while Indium increases the compressive strain in the active region or decreases the energy gap. Unfortunately, a high Aluminum content leads to alloy scattering and lowers the carrier confinement in the active region. On the other hand, an increasing Indium content requires a reduction of the growth temperature and a higher V/III ratio. This means that only wave lengths between 1.3 and 2.2 µm can be achieved with relative high gain and a low photoluminescence linewidth [10].

The quaternary material system AlGaInAs lattice matched to InP for 1.5 µm emission wavelength provides good electron confinement in the active region thanks to its high $\Delta E_c/\Delta E_g$ ratio, compared with the almost equivalent material system GaInAsP. Furthermore, comprising only one group-V element, AlGaInAs grown with solid source MBE enables sharp interfaces and gives the possibility of implementing very high strain in the active region (up to 2%). The required thickness of an 1.5-µm AlGaInAs QW with 7-nm thick $Al_{0.274}Ga_{0.203}In_{0.523}As$ barrier is plotted in Fig. 2.1 versus the Aluminium mole fraction and for compressive strain ranging from 1.2 to 2.0%, generated by increasing the Indium content. Assuming an active region with 8 QWs to enhance the differential gain [11], the lateral shaded area represents thickness-strain combinations which exceed the dislocation-free critical thickness [12]. Under the same assumption, the upper shaded area would lead to an active region thicker than one quarter of the emission wavelength, which means a negligible increase of confinement factor at the cost of high threshold current density. The thickness of the QWs can be optimized within these boundaries.

2.1.2 Hybrid-Cavity Concepts

A common approach used to boost the small-signal modulation bandwidth of semiconductor lasers is the reduction of the photon lifetime. On one hand, the

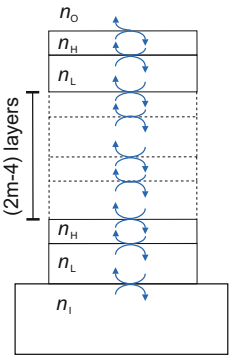

Fig. 2.2 Schematic of a DBR with quarter-wave stacks of layers with pairwise varying refractive index

relaxation resonance frequency of VCSELs is inversely proportional to the square root of the photon lifetime. On the other hand, the damping increases proportionally to the square of the relaxation resonance frequency, and the slope of its growth is proportional to the photon lifetime. The different approaches used to decrease the photon lifetime are the increase of mirror losses [13, 14] or the reduction of the effective cavity length [2, 15]. The last approach is the subject of this subsection. A hybrid dielectric/semiconductor cavity is introduced where a semiconductor cavity is combine with dielectric DBRs to achieve a strong confinement of the field in the active region.

DBRs are quarter-wave stacks of layers with alternating refractive index, as shown schematically in Fig. 2.2. The light is incident from a medium with refractive index n_I and penetrates in a DBR made of m layers with alternating low and high refractive indexes n_L and n_H. The light is than outcoupled to a medium with an index n_O. The *phase penetration depth* is defined as the depth at which the optical field appears to be reflected by a constant-phase mirror. It is common practice to define the *energy penetration depth* as the depth at which the energy density falls to $1/e$ of its initial value. These definitions give similar results for a large number of mirror pairs or for an outcoupling interface with high refractive index ratio. The reflection delay time τ_m of a DBR with $m/2$ pairs at the Bragg frequency f_B is given from the exact relation [16]:

$$\tau_m = \frac{1}{2f_B} \cdot \frac{q}{1-p} \cdot \frac{(1-a^2p^{m-1})(1-p^m)}{(1-q^2a^2p^{2m-2})} \tag{2.1}$$

where

$$q = \frac{n_L}{n_I}, p = \frac{n_L}{n_H}, a = \frac{n_O}{n_H}. \tag{2.2}$$

The optical phase penetration depth L_τ is defined as $nL_\tau = c\tau_m/2$ where n is assumed, for simplicity, to be a common refractive index of the cavity. The optical phase penetration depth is plotted in Fig. 2.3 as a function of the difference between

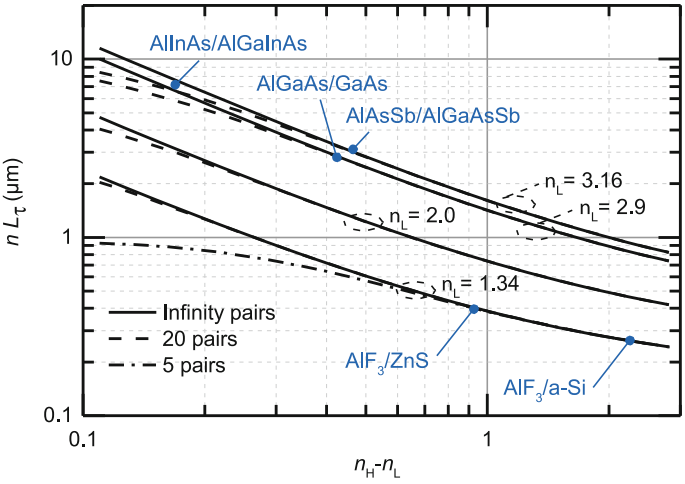

Fig. 2.3 Optical phase penetration depth in a DBR as a function of the difference between the refractive indexes of the two mirror's material for different n_L and for fixed values $n_I = 3.16$ and $n_O = 1.00$ at the Bragg wavelength of 1.55 μm for infinite number of layers (*solid line*), 20 pairs (*dash line*) and 5 pairs (*dash-dot line*). Commonly used material' pairs for DBRs are shown

the refractive indexes of the two mirror's materials and for different refractive indexes n_L. This plot refers to DBRs placed on top of InP and outcoupling to air, and designed at the Bragg wavelength of 1.55 μm. It gives a nice overview of the penetration depth linked to several DBR' material systems. Properly chosen dielectric DBRs, such as AlF_3/Si, have optical penetration depths that are one order of magnitude shorter than semiconductor ones, such as AlInAs/AlGaInAs.

The DBRs commonly used for GaAs-based VCSELs consist of binary and ternary semiconductor compounds such as AlAs and AlGaAs alloys. They offer several advantages such as high refractive-index contrast between the layers and low thermal resistivity. Semiconductor DBRs for InP-based devices are instead based on ternary and quaternary compounds such as AlInAs and AlGaInAs alloys, which have low refractive-index contrast that is long propagation depth, and high thermal resistivity. The latter is due to phonon-phonon interactions and phonon scattering with lattice defects, and increases with the number of foreign atoms added to a host lattice [10]. AlGaAsSb/AlAsSb DBRs latticed-matched to InP offer a higher refractive-index contrast but have poor electrical and thermal conductivities [17]. Different approaches such as InP/air-gaps [18] or dielectric DBRs [2] have been explored to shorten the propagation length of the field in the mirror, but the low thermal conductivity of those DBRs challenges the VCSEL's stationary and dynamic performance. In order to overcome this limitation, wafer-fused AlGaAs/GaAs DBRs have been demonstrated to combine high-refractive index contrast and low thermal resistance [19].

An alternative to DBRs are high-contrast gratings (HCGs). A HCG is a near-wavelength grating made of a high refractive-index material and surrounded

by a low-index material. 1.55-μm InP-based HCG VCSELs feature broadband and high reflectivity for surface-normal incident light with field polarization that can be designed to be either parallel or orthogonal to the elongated elements of the grating [20].

2.1.3 Tunnel-Junction Laser

For energy-efficient and single-mode operation, current and optical field have to be confined such that the fundamental optical mode is electrically excited, and optical losses are minimized. Both current and optical confinement can be achieved in VCSELs by means of current apertures realized by structured buried tunnel junctions (BTJ).

For GaAs-based VCSELs, a current aperture is typically achieved through radial *selective oxidation* of $Al_xGa_{1-x}As$ layers where x is near to 0.98 [21]. The oxidation rate changes by more than two orders of magnitude by varying x from 0.8 to 1 [22]. The large lattice constant mismatch between AlGaAs alloy and InP prevents the integration of this material system on InP-based long wavelength devices. The related material system $Al_xIn_{1-x}As$ is lattice matched to InP for $x = 0.5$, leading to a low oxidation rate. Furthermore, the AlInAs native oxide differs from that reported for AlGaAs due to the composite structure of the oxide related to the low Al content [23]. Another technique used to achieve current confinement in GaAs- and InP-based devices is *ion implantation*, which produces highly resistive regions in the semiconductor cavity. These VCSELs present the advantage of a planar device geometry. However, the lack of inherent optical confinement can lead to varying threshold and modulation limitations [24].

For InP-based VCSELs, tunnel junctions consisting of p^+-AlGaInAs and n^+-GaInAs have been demonstrated [25]. Current and optical confinement are achieved by etching the n^+-layer of the tunnel junction in circular-shaped areas and re-growing with n-InP to match the desired cavity length as shown in Fig. 2.4a. The etched area acts as a reverse biased pn-junction enabling current confinement to the *not* etched area. The band diagrams for the tunnel and blocking junctions are plotted in Fig. 2.4b and c, respectively. This method offers the great advantage of defining the aperture by simple optical lithography but raises the challenges related to re-grow of the structured junction. Re-growing with solid source MBE will *not* flatten the etched structure, which is reproduced at the upper mirror/semiconductor interface. The effect will be an effective fiber-like waveguiding with refractive index contrast Δn_{eff} depending on the height of the overgrown tunnel junction (ΔL):

$$\frac{\Delta n_{eff}}{n_{eff}} = \frac{\Delta L}{L}, \tag{2.3}$$

where L is the cavity length and n_{eff} is the effective refractive index [26]. Corresponding to the diameter of the fiber's core, the diameter of the tunnel junction will

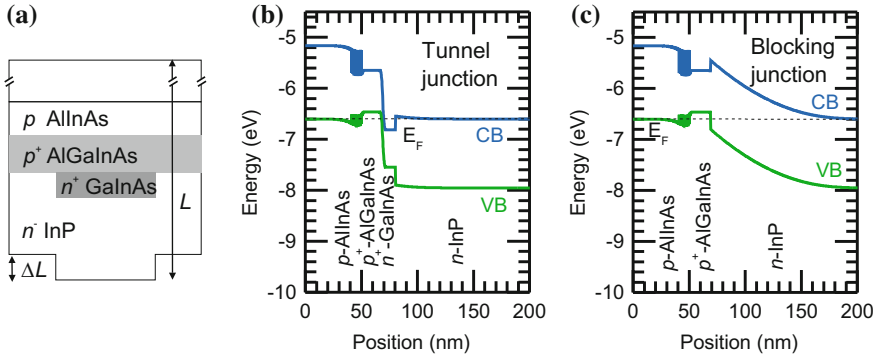

Fig. 2.4 **a** Schematic cross-section of a BTJ. Simulated band diagram **b** of a p^+-AlGaInAs/n^+-GaInAs tunnel junction, and **c** of a reverse-biased p^+-AlGaInAs/n-InP diode

determine how many transverse modes can propagate in the cavity. Single mode operation and high output power can be achieved by choosing this diameter sufficiently small as will be shown in the next section.

One of the main advantages of a tunnel junction is the reduction of the series resistance of VCSELs. The active region of long-wavelength VCSELs is typically embedded between an *n*-InP and a *p*-AlInAs, which, due to their band offset, offer effective carrier confinement to the active region. However, the poor electrical, thermal and optical properties of AlInAs motivate the need for reducing its thickness. This can be achieved by means of a low-resistive tunnel junction allowing to reduce the thickness of the AlInAs layer to less than one quarter of the emission wavelength, and to match the desired total cavity length using low-resistive *n*-InP instead.

2.2 Single-Mode 1.55-µm Short-Cavity VCSELs

Short-reach communication links and networks can employ 850-nm or 980-nm VCSELs, which emit typically in multiple transverse modes. However, signals carried by fundamental transverse modes with narrow linewidths can be transmitted over longer distances by limiting the chromatic dispersion of the fiber. For this reason, access and metropolitan networks are established on single-mode fiber motivating the need for single-mode 1.3- and 1.55-µm VCSELs.

The historical growth of the small-signal modulation bandwidth of short- and long-wavelength VCSELs is shown in Fig. 2.5. While short-wavelength devices have achieved bandwidths up to 30 GHz [1] by 2015, long-wavelength VCSELs show inferior modulation capabilities. The technological issues related to the bandwidth scaling of InP-based devices have been discussed in Sect. 2.1 and are related to the lack of semiconductor DBRs with low thermal resistivity, high

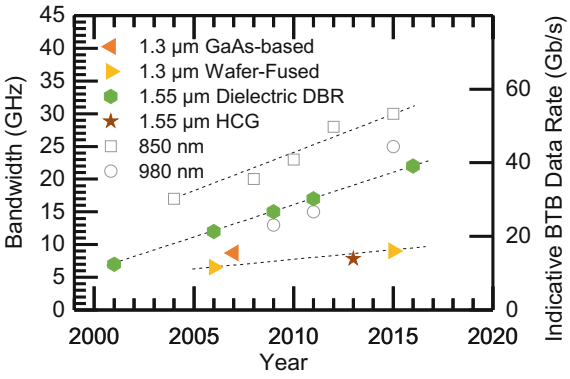

Fig. 2.5 Temporal evolution of the small-signal bandwidth for 1.3- and 1.55-μm VCSEL. For comparison, GaAs-based VCSELs are included (grey)

electrical conductivity and high refractive index contrast. The long-wavelength VCSELs, which have shown the highest modulation capabilities, belong to the family of devices using the hybrid dielectric-semiconductor cavities [3]. While they have the great advantage of a reduced effective cavity length compared to their semiconductor counterpart, they challenge the thermal and electrical management.

In this section, the stationary and dynamic characteristics of 1.55-μm VCSELs with single-mode hybrid dielectric-semiconductor cavities are reviewed.

2.2.1 *Hybrid Dielectric-Semiconductor VCSELs*

A schematic image of an InP-based VCSEL with dielectric DBRs is shown in Fig. 2.6a. This device has a cavity length which is three time the laser's emission wavelength (3-λ cavity) and it is encapsulated in an electrical passivation polymer. The field intensity and refractive index profile along the same cavity is shown in Fig. 2.6b.

The VCSEL's active region consists of eight compressively strained AlGaInAs quantum wells embedded between a *n*-doped InP layer and a *p*-doped AlInAs cladding layer. Current confinement is achieved by a circularly shaped p^+-AlGaInAs/n^+-GaInAs buried tunnel junction. The outcoupling mirror consists of a dielectric AlF_3/ZnS distributed Bragg reflector with 99.3% reflectivity, while the bottom mirror consists of a hybrid metal-dielectric Au-AlF_3/ZnS DBR with reflectivity of 99.9%. Furthermore, passivation with benzocyclobutene (BCB) reduces both chip and contact pad parasitic.

Dielectric DBRs are poor electrical and thermal conductors. Therefore, the heat generated in the VCSEL cavity flows radially across the overgrown InP, around the DBR, and it is drained out by means of the Gold anode which works as an heat sink. This three-dimensional problem can be simplified to a one-dimensional problem by solving the Fourier law for cylindrical coordinates, which lead to a thermal spreading resistance:

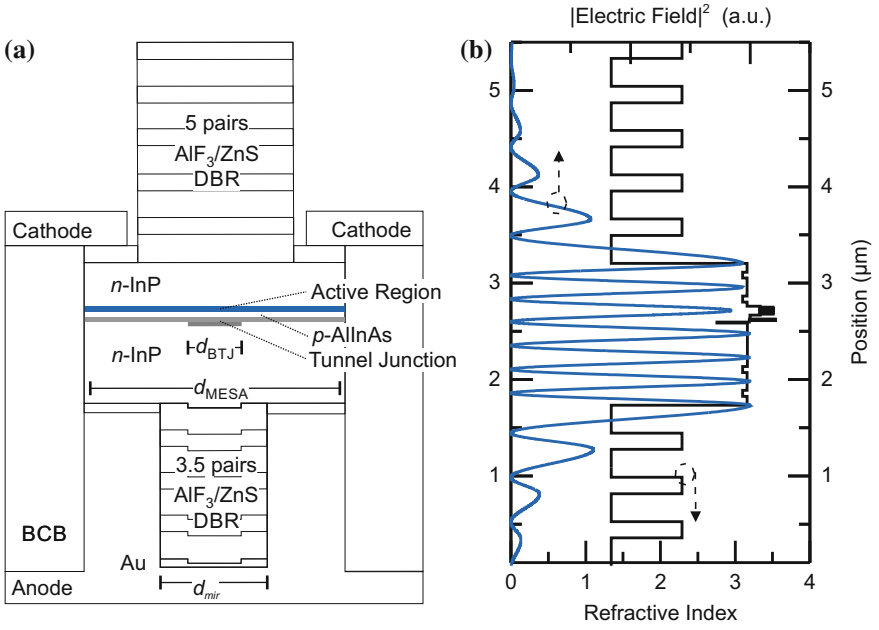

Fig. 2.6 **a** Schematic image of a 3-λ cavity InP-based VCSEL with dielectric DBRs encapsulated inside an electrical passivation polymer. **b** Field intensity and refractive index profile inside a 3-λ 1550-nm VCSEL

$$R_{\mathrm{th}} = \frac{\rho_{\mathrm{th}}}{2\pi L_{\mathrm{th}}} \ln\left(\frac{d_{\mathrm{mir}}}{d_{\mathrm{BTJ}}}\right) \tag{2.4}$$

where ρ_{th} is the thermal resistivity, and L_{th} is the thickness of the heat spreading layer, and the thermal resistance. Analogously, the electrical current has to flow radially across the two DBRs to reach the tunnel junction and the active region experiencing an electrical spreading resistance R_{el}. While small diameters of the DBRs are beneficial for the electrical and thermal resistance of the VCSEL, a lower bound to the diameter is given by the optical beam waist. In other words, the DBR has to be large enough to provide the desired reflectivity to the guided mode.

2.2.2 *Stationary Characteristics*

Optical and electrical stationary characteristics of VCSELs are strongly determined by the diameter of the tunnel junction. Large diameters lead to low serial resistances but allow several transversal modes to propagate within the VCSEL.

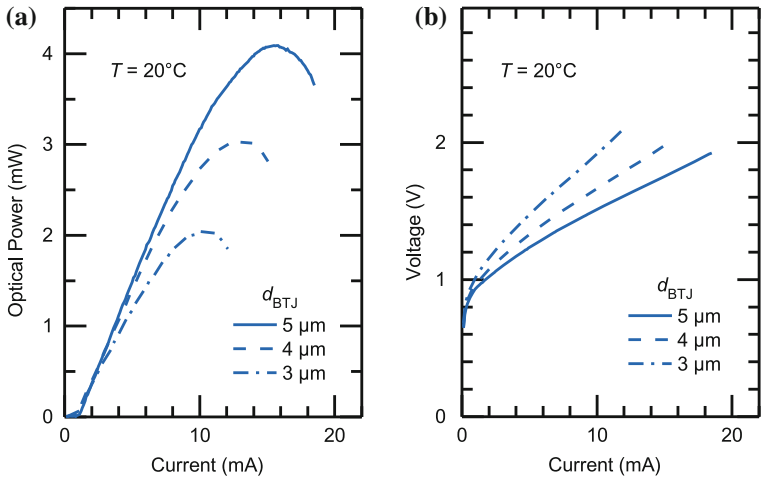

Fig. 2.7 **a** Emitted optical power versus bias current and **b** voltage versus applied current of a 1.55-μm VCSEL with diameter of the tunnel junction of 3, 4, and 5 μm at 20 °C

The output power versus the current for a 1.55-μm VCSEL is shown in Fig. 2.7a for devices with 3-, 4- and 5-μm diameter of the tunnel junction. The effectively pumped volume increases with the diameter of the current aperture leading to higher optical output power. The voltage-current characteristics are shown in Fig. 2.7b showing that the differential resistance decreases with increasing diameter of the tunnel junction. This is due to the increasing serial and spreading resistances which are proportional to $1/d_{\mathrm{BTJ}}^2$ and as ln $(d_{\mathrm{mir}}/d_{\mathrm{BTJ}})$, respectively.

For a VCSEL with aperture diameter of 5 μm, the power-current characteristics are plotted in Fig. 2.8a for different heat-sink temperatures ranging from 5 to 90 °C. Figure 2.8b shows the voltage drop across the VCSEL in the same temperature range displaying only weak temperature dependence with a slight decrease for high temperatures. The threshold current of a semiconductor laser is related to its high-speed performances. This is because the relaxation resonance frequency is proportional to the square root of the current relative to threshold [27]. In other words, lower thresholds are beneficial because they yield relaxation resonance frequencies with a lower current, that is, lower internal temperature. Figure 2.8c shows the threshold current as a function of the heat-sink temperature for three devices with 3-, 4- and 5-μm aperture diameter. The mode-gain offset was chosen to yield minimum threshold current at room temperature. For the same laser, the differential quantum efficiency is plotted as a function of heat-sink temperature in Fig. 2.8d. As can be seen, for smaller BTJs, the differential quantum efficiency decreases. This is due to diffraction effects and to the week confinement of the transversal modes propagating in the longitudinal direction [28].

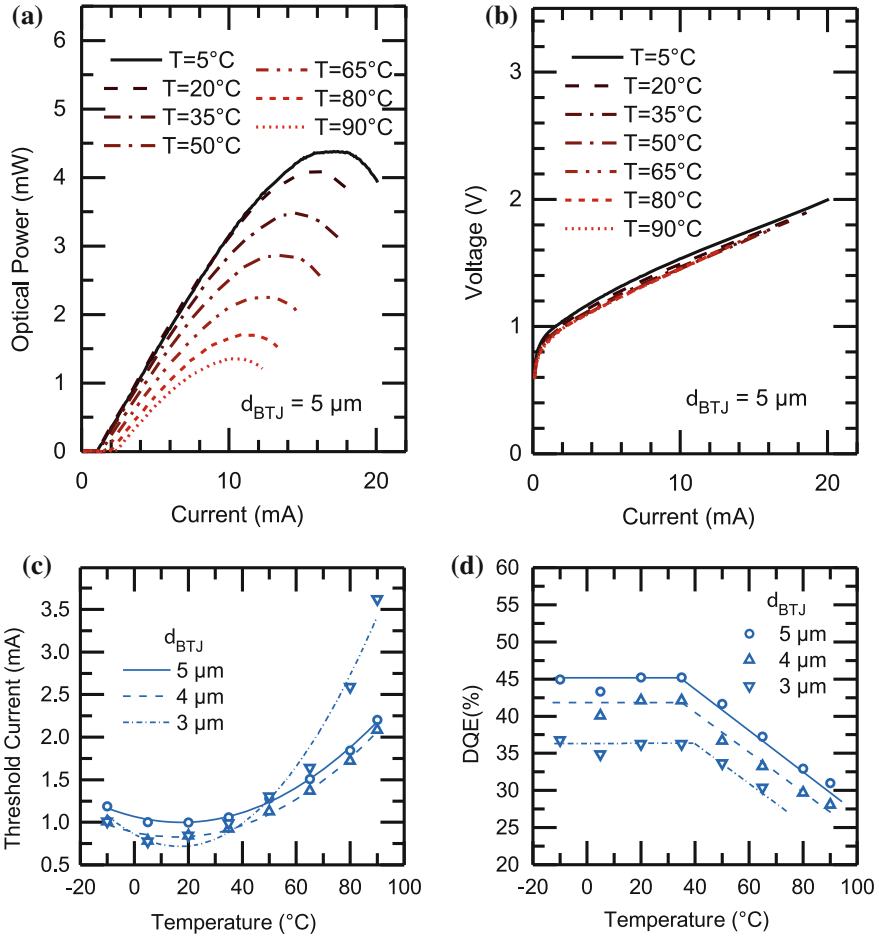

Fig. 2.8 **a** Emitted optical power and **b** voltage as a function of the bias current for a VCSEL with tunnel junction diameter of 5 µm operated at heat sink temperatures between 5 and 90 °C. **c** Threshold current and **d** differential quantum efficiency versus heat sink temperature for three different VCSELs with diameter of the tunnel junction of 3, 4 and 5 µm

Figure 2.9a shows the dissipated power and the wall-plug efficiency versus bias current measured at different heat-sink temperatures. While the dissipated power increases with the square of the applied current, the wall-plug efficiency has a maximum of 39% at 5 mA and at 20 °C. Finally, the room temperature optical spectrum of the same VCSEL is shown in Fig. 2.9b. This shows that, for diameters up to 5 µm, single mode operation with side mode suppression ratios above 40 dB can be achieved.

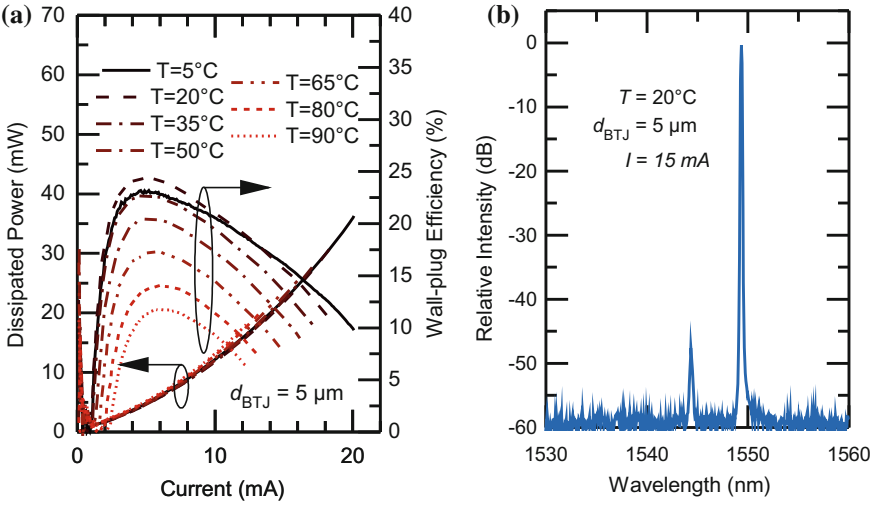

Fig. 2.9 **a** Dissipated power and wall-plug efficiency versus bias current for heat sink temperatures ranging from 5 to 90 °C. **b** Room temperature optical spectrum of a VCSEL at roll-over current with tunnel junction diameter of 5 µm

2.2.3 *Dynamic Characteristics*

The VCSEL's small-signal modulation response is determined by the combination of intrinsic and parasitic effects [29]. The overall modulation frequency response is given by a three-pole transfer function depending on the relaxation resonance frequency ν_R, the intrinsic damping factor γ and the parasitic cut-off frequency ν_p.

The VCSEL's small-signal modulation response was measured with a vector network analyzer for different bias currents. For an aperture of 5 µm and a 3-λ long semiconductor cavity length, a small-signal modulation bandwidth in excess of 17 GHz is achieved for a bias current of 10.4 mA and a DC electrical-power consumption of 16 mW, respectively, as shown in Fig. 2.10a. The relaxation resonance frequency versus the square root of current relative to threshold is plotted in Fig. 2.10b. The highest value achieved is 19 GHz. In Fig. 2.10c, γ is plotted versus ν_R^2. In the region where self-heating is small, the curve has a linear behavior with a slope K. The K-factor defines the maximum intrinsic capabilities of the laser and is proportional to the photon life time [27].

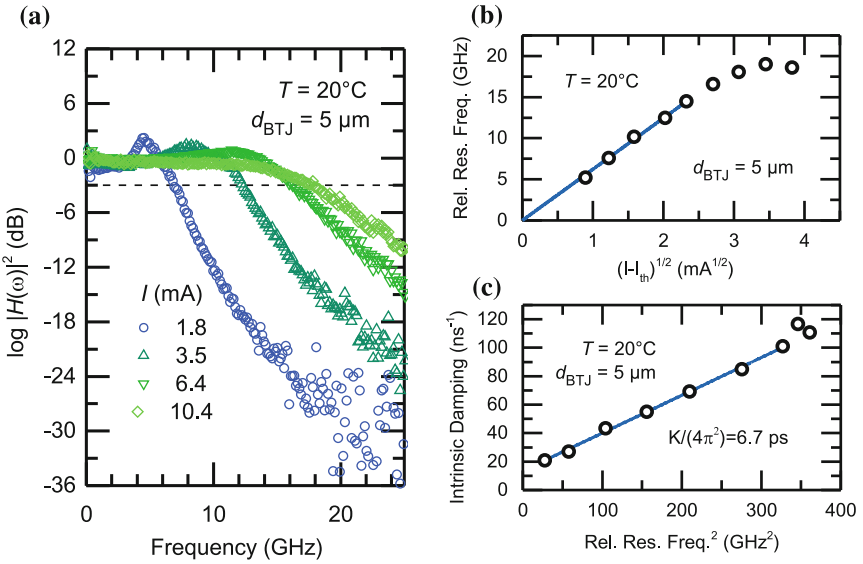

Fig. 2.10 For a 1.55-μm VCSEL with $d_{BTJ} = 5$ μm operated at room temperature: **a** small-signal modulation response, **b** relaxation resonance frequency versus the square root of current relative to threshold, and **c** intrinsic damping versus squared relaxation resonance frequency

2.3 VCSEL Arrays and Advanced Modulation Formats

Long-wavelength VCSELs find applications in datacom and telecom networks thanks to the low optical attenuation of silica optical fibers. The small-signal modulation bandwidth is a common measure to quantify the high-speed capability of a semiconductor laser and the amount of data that can be transmitted depends on transmission distance, and modulation techniques. Furthermore, forward error correction (FEC) can also be used to boost the transmitted data.

In this section, we review data transmission experiments performed by using 1.5-μm 17-GHz VCSELs whose design and stationary performances are analogue to the one presented in Sect. 2.2. An overview of the large-signal modulation data rates and transmission lengths achieved with different transmission formats and detection schemes is presented in Table 2.1, and it will be discussed in this section.

2.3.1 Data Communication

Optical interconnect for intra data center applications must cover distances of few hundred meters and fulfill the need for low power, low cost and high density [36]. Long-wavelength VCSELs, thanks to the low losses in the SMF, are particularly attractive in large datacenters where links longer than 200 m are required. The

Table 2.1 Large-signal modulation net data rates and transmission lengths achieved with different transmission formats and detection schemes using single 1.5-μm VCSELs with small-signal bandwidth of approximately 17 GHz

VCSEL net bit rate (Gb/s)	SMF Length (km)	Modulation format	Transmitter	Detection	References
10	17.3	NRZ	DAC	Direct	[30]
25	4.2	NRZ	DAC	Direct	[2]
35	BTB	NRZ	DAC	Direct	[2]
40	1	4-PAM	0.13 μm SiGe BiCMOS	Direct	[31]
42	400	4-PAM	DAC	Choerent (20% SD-FEC)	[32]
44	960[a]	3-PAM	DAC	Choerent (20% HD-FEC)	[33]
50	2	NRZ	0.13 μm SiGe BiCMOS	Direct	[34]
56	BTB	NRZ	0.13 μm SiGe BiCMOS	Direct	[34]
79	4	DMT	72 GS/s DAC	Direct (20% HD-FEC)	[35]
88	0.5	DMT	72 GS/s DAC	Direct (20% HD-FEC)	[35]
96	BTB	DMT	72 GS/s DAC	Direct (20% HD-FEC)	[35]

[a]EDFA + DGEF

bit-error rate experiments described in this section refers to VCSELs with emission in the C-band, small-signal bandwidth of approximately 17 GHz and the design presented in Sect. 2.2.

In datacom networks, the need for low-latency and energy-effective links motivates the use of non-return-to-zero (NRZ) modulation. The highest bandwidth demonstrated with this modulation format in back-to-back (BTB) configuration is 56 Gb/s [34]. In this experiment, the electrical signal was generated by a 0.13-μm BiCMOS driver with 2-tap feed-forward equalization (FFE) and neither FEC nor digital-signal-processing (DSP) were used.

Using direct detection and advanced modulation formats such as 4-level pulse-amplitude modulation (4-PAM), net bit rates in excess of 40 Gb/s are transmitted over 1 km of single-mode fiber (SMF). These results were achieved by means of a energy-efficient 0.13 μm SiGe BiCMOS driver with 2-tap FFE architecture [31].

In order to make full use of the bandwidth of the transmission link, discrete multi-tone (DMT) and direct detection is a suitable candidate for short-reach high-density optical links. With this modulation format, 96-Gb/s net bit rate have been demonstrated in BTB configuration [35].

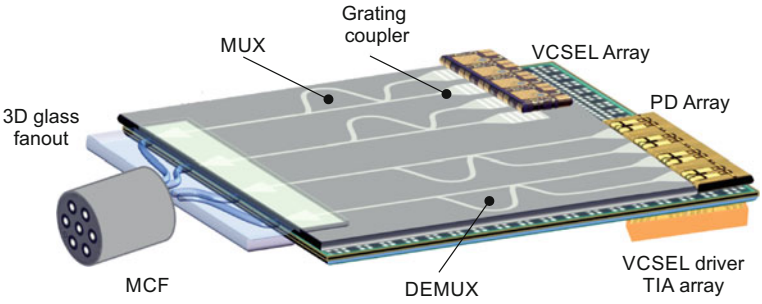

Fig. 2.11 Schematic of a 3D photonic and electronic silicon-on-insulator transceiver based on long-wavelength VCSELs arrays capable of terabits connectivity [37]

With device's data rate limited to a few tens of gigabits, terabit links are achieved by means of aggregate bandwidth. A 3D photonic and electronic silicon-on-insulator (SOI) transceiver based on long-wavelength VCSEL arrays and capable of terabits connectivity is depicted in Fig. 2.11 [37]. In this approach, a VCSEL array emitting at two different wavelengths is heterogeneously integrated to a SOI platform. The emitted light is coupled into a planar silicon waveguide by means of a grating coupler array. Pairs of signals with different wavelengths are multiplexed (MUX) to a single SOI's core and, later, coupled to the core of a multi core fiber (MCF) by means of a glass interface. Optical signals coming to the transceiver are demultiplexed (DEMUX) and read out by an array of photodiodes.

2.3.2 Telecommunication

Telecom access networks cover distances of several tens of kilometer. With the introduction of technologies such as fiber-to-the-house (FTTH), long-wavelength VCSELs have achieved increasing relevance in this area [38]. Metro and regional networks require links of the order of several hundreds of kilometers. In addition to the signal attenuation, metro fibers could have high polarization-mode dispersion (PMD) and large variations of chromatic dispersion (CD) compared to the access networks [39].

Single-mode 1.5-μm VCSELs have enabled 10 Gb/s transmission over 17 km through SSMF and using direct detection [30]. Furthermore, digital coherent detection at the receiver allows the recovery of the amplitude and phase of an optical carrier and the compensation by using DSP of CD and PMD. The combination of digital coherent detection and 4-PAM and 3-PAM results in net bit rates in excess of 40 Gb/s and transmission distances typical of metro networks (several hundreds of kilometers). A digital to analog converter (DAC) is used to generate these multi-level PAM signals. The longest distance achieved with this system is 960 km where a 4 × 80 km Erbium-doped-fiber amplifier (EDFA) recirculating

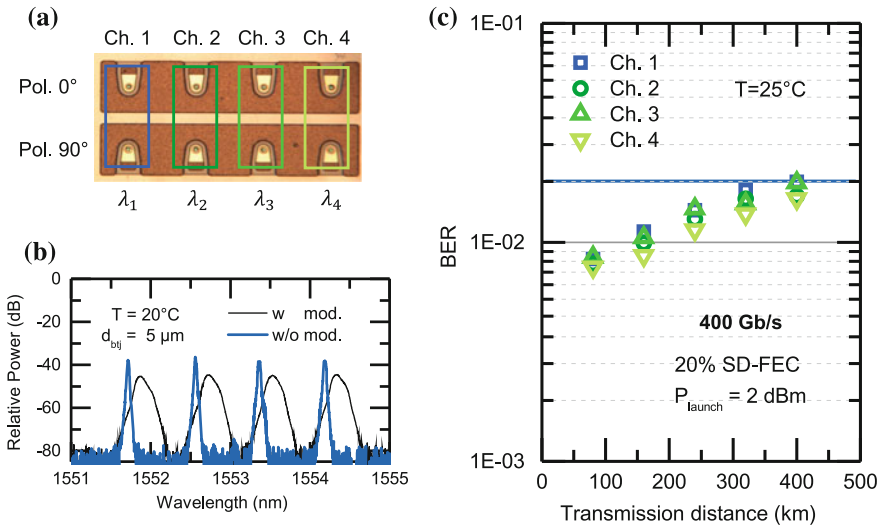

Fig. 2.12 **a** Microscope image of a 2 × 4 VCSEL array. **b** Spectrum of eight VCSELs emitting in four 100-GHz spaced channels transmitting two perpendicularly polarized signals. **c** BER versus transmission distance for the four channels transmission two perpendicularly polarized signals

loops are alternated with a dynamic gain equalization filter (DGEF) to block amplified spontaneous emission, and with an EDFA [33].

In Fig. 2.12a, a microscope image of a 2 × 4 VCSEL array is shown [32]. The array emits at four different wavelengths. The emission spectrum of the eight VCSELs consists of four 100-GHz spaced channels carrying two externally perpendicularly polarized 4-PAM signals as shown in Fig. 2.12b. These signals are detected with digital coherent detection, which enabled polarization DEMUX and compensation of CD, PMD and other impairments using DSP in the electrical domain. In Fig. 2.12c, the bit error rate (BER) versus transmission distance is shown for each of the four channels. A net information bit rate of 333 Gb/s is transmitted over 400-km SSMF assuming 20% overhead soft-decision forward-error-correction (SD-FEC) [32].

2.4 Conclusion

In this chapter, InP-based VCSELs have been studied with focus on the active region design, cavity length engineering, and current and optical confinement. Despite those arguments apply to all InP-based VCSELs with emission wavelength between 1.3 and 2.0 µm, stationary and dynamic characteristics are presented for a 1.55 µm VCSEL. Finally, datacom and telecom transmission experiments have been presented.

Acknowledgements This work was partially supported by the European Commission through the FP7 project MIRAGE (ref. 318228).

References

1. E. Haglund, P. Westbergh, J.S. Gustavsson, E.P. Haglund, A. Larsson, M. Geen, A. Joel, 30 GHz bandwidth 850 nm VCSEL with sub-100 fJ/bit energy dissipation at 25–50 Gbit/s. Electron. Lett. **51**(14), 1096–1098 (2015)
2. M. Müller, W. Hofmann, T. Grundl, M. Horn, P. Wolf, R.D. Nagel, E. Ronneberg, G. Böhm, D. Bimberg, M.-C. Amann, 1550-nm high-speed short-cavity VCSELs. IEEE J. Sel. Top. Quantum Electron. **17**(5), 1158–1166 (2011). doi:10.1109/JSTQE.2011.2109700
3. S. Spiga, D. Schoke, A. Andrejew, M. Müller, G. Boehm, M.-C. Amann, Single-Mode 1.5-μm VCSELs with 22-GHz small-signal bandwidth, in *Optical Fiber Communication Conference*, Anaheim, California, 20 Mar 2016. OSA Technical Digest (online) (Optical Society of America, 2016), p. Tu3D.4. doi:10.1364/OFC.2016.Tu3D.4
4. P. Sundgren, R. Marcks von Wurtemberg, J. Berggren, M. Hammar, M. Ghisoni, V. Oscarsson, E. Odling, J. Malmquist, High-performance 1.3 μm InGaAs vertical cavity surface emitting lasers. Electron. Lett. **39**(15), 1128–1129 (2003). doi:10.1049/el:20030733
5. H. Riechert, A. Ramakrishnan, G. Steinle, Development of InGaAsN-based 1.3 μm VCSELs. Semicond. Sci. Technol. **17**(8), 892 (2002)
6. J.A. Lott, N.N. Ledentsov, V.M. Ustinov, N.A. Maleev, A.E. Zhukov, A.R. Kovsh, M.V. Maximov, B.V. Volovik, Z.I. Alferov, D. Bimberg, InAs-InGaAs quantum dot VCSELs on GaAs substrates emitting at 1.3 μm. Electron. Lett. **36**(16), 1384–1385 (2000). doi:10.1049/el:20000988
7. Y. Arakawa, A. Yariv, Theory of gain, modulation response, and spectral linewidth in AlGaAs quantum well lasers. IEEE J. Quantum Electron. **21**(10), 1666–1674 (1985). doi:10.1109/JQE.1985.1072555
8. I. Suemune, Theoretical study of differential gain in strained quantum well structures. IEEE J. Quantum Electron. **27**(5), 1149–1159 (1991). doi:10.1109/3.83371
9. A.R. Adams, Strained-layer quantum-well lasers. IEEE J. Sel. Top. Quantum Electron. **17**(5), 1364–1373 (2011). doi:10.1109/JSTQE.2011.2108995
10. G. Böhm, R. Shau, R. Meyer, M.C. Amann, M. Ortsiefer, J. Rosskopf, F. Mederer, InP-based VCSEL technology covering the wavelength range from 1.3 to 2.0 μm. Paper presented at the 2002 International Conference on Molecular Beam Epitaxy, 15–20 Sept 2002
11. B. Zhao, T.R. Chen, A. Yariv, The extra differential gain enhancement in multiple-quantum-well lasers. IEEE Photonics Technol. Lett. **4**(2), 124–126 (1992). doi:10.1109/68.122336
12. M. Gendry, V. Drouot, C. Santinelli, G. Hollinger, Critical thicknesses of highly strained InGaAs layers grown on InP by molecular beam epitaxy. Appl. Phys. Lett. **60**(18), 2249–2251 (1992). doi:10.1063/1.107045
13. D. Ellafi, V. Iakovlev, A. Sirbu, S. Grigore, Z. Mickovic, A. Caliman, A. Mereuta, E. Kapon, Effect of cavity lifetime variation on the static and dynamic properties of 1.3-μm wafer-fused VCSELs. IEEE J. Sel. Top. Quantum Electron. **21**(6), 1–9 (2015). doi:10.1109/JSTQE.2015.2412495
14. P. Westbergh, J.S. Gustavsson, B. Kögel, A. Haglund, A. Larsson, Impact of photon lifetime on high-speed VCSEL performance. IEEE J. Sel. Top. Quantum Electron. **17**(6), 1603–1613 (2011). doi:10.1109/JSTQE.2011.2114642
15. K.Y. Lau, A. Yariv, Ultra-high speed semiconductor lasers. IEEE J. Quantum Electron. **21**(2), 121–138 (1985). doi:10.1109/JQE.1985.1072624

16. D.I. Babic, S.W. Corzine, Analytic expressions for the reflection delay, penetration depth, and absorptance of quarter-wave dielectric mirrors. IEEE J. Quantum Electron. **28**(2), 514–524 (1992). doi:10.1109/3.123281
17. S. Nakagawa, E. Hall, G. Almuneau, J.K. Kim, D.A. Buell, H. Kroemer, L.A. Coldren, 1.55-μm InP-lattice-matched VCSELs with AlGaAsSb-AlAsSb DBRs. IEEE J. Sel. Top. Quantum Electron. **7**(2), 224–230 (2001). doi:10.1109/2944.954134
18. L. Chao-Kun, D.P. Bour, Z. Jintian, W.H. Perez, M.H. Leary, A. Tandon, S.W. Corzine, M.R. T. Tan, High temperature continuous-wave operation of 1.3- and 1.55-μm VCSELs with InP/air-gap DBRs. IEEE J. Sel. Top. Quantum Electron. **9**(5), 1415–1421 (2003). doi:10.1109/JSTQE.2003.820924
19. A. Syrbu, A. Mircea, A. Mereuta, A. Caliman, C.A. Berseth, G. Suruceanu, V. Iakovlev, M. Achtenhagen, A. Rudra, E. Kapon, 1.5-mW single-mode operation of wafer-fused 1550-nm VCSELs. IEEE Photonics Technol. Lett. **16**(5), 1230–1232 (2004). doi:10.1109/LPT.2004.826099
20. R. Yi, Y. Weijian, C. Chase, M.C.Y. Huang, D.D.P. Worland, S. Khaleghi, M.R. Chitgarha, M. Ziyadi, A.E. Willner, C.J. Chang-Hasnain, Long-wavelength VCSEL using high-contrast grating. IEEE J. Sel. Top. Quantum Electron. **19**(4), 1701311–1701311 (2013). doi:10.1109/JSTQE.2013.2246780
21. K.D. Choquette, K.M. Geib, H.C. Chui, H.Q. Hou, R. Hull, Selective oxidation of buried AlGaAs for fabrication of vertical-cavity lasers. MRS Online Proc. Libr. Arch. **421**, 53 (1996). doi:10.1557/PROC-421-53
22. K.D. Choquette, R.P. Schneider Jr., K.L. Lear, K.M. Geib, Low threshold voltage vertical-cavity lasers fabricated by selective oxidation. Electron. Lett. **30**(24), 2043–2044 (1994). doi:10.1049/el:19941421
23. P. Petit, P. Legay, G. Le Roux, G. Patriarche, G. Post, M. Quillec, Controlled steam oxidation of AlInAs for microelectronics and optoelectronics applications. J. Electron. Mater. **26**(12), L32–L35 (1997). doi:10.1007/s11664-997-0065-0
24. C.W. Wilmsen, H. Temkin, Vertical-Cavity Surface-Emitting Lasers: Design, Fabrication, Characterization, and Applications, vol. 24 (Cambridge University Press, 2001)
25. M. Ortsiefer, R. Shau, G. Böhm, F. Köhler, G. Abstreiter, M. Christian-Amann, Low-resistance InGa(Al)As tunnel junctions for long wavelength vertical-cavity Surface-emitting Lasers. Jpn. J. Appl. Phys. **39**(4R), 1727 (2000)
26. G. Hadley, K. Lear, M. Warren, K. Choquette, J. Scott, S. Corzine, Comprehensive numerical modeling of vertical-cavity surface-emitting lasers. IEEE J. Quantum Electron. **32**(4), 607–616 (1996)
27. L.A. Coldren, S.W. Corzine, M.L. Mashanovitch, Diode Lasers and Photonic Integrated Circuits, vol. 218 (Wiley, 2012)
28. R. Burton, M. Stern, P. Kendall, P. Robson, Modelling of diffraction in pillar vertical cavity surface-emitting lasers with embedded Bragg layers. Opt. Quant. Electron. **28**(11), 1677–1684 (1996)
29. R.S. Tucker, High-speed modulation of semiconductor lasers. IEEE Trans. Electron Devices **32**(12), 2572–2584 (1985)
30. M.C. Amann, E. Wong, M. Müller, Energy-efficient high-speed short-cavity VCSELs. Paper presented at the Optical Fiber Communication Conference and Exposition (OFC/NFOEC), 2012 and the National Fiber Optic Engineers Conference, 4–8 Mar 2012
31. W. Soenen, R. Vaernewyck, Y. Xin, S. Spiga, M.C. Amann, K.S. Kaur, P. Bakopoulos, J. Bauwelinck, 40 Gb/s PAM-4 transmitter IC for long-wavelength VCSEL links. IEEE Photonics Technol. Lett. **27**(4), 344–347 (2015). doi:10.1109/LPT.2014.2372041
32. C. Xie, S. Spiga, P. Dong, P. Winzer, M. Bergmann, B. Kögel, C. Neumeyr, M.C. Amann, 400-Gb/s PDM-4PAM WDM system using a monolithic 2 × 4 VCSEL array and coherent detection. J. Lightwave Technol. **33**(3), 670–677 (2015). doi:10.1109/JLT.2014.2363017
33. C. Xie, P. Dong, P. Winzer, C. Gréus, M. Ortsiefer, C. Neumeyr, S. Spiga, M. Müller, M.C. Amann, 960-km SSMF transmission of 105.7-Gb/s PDM 3-PAM using directly modulated

VCSELs and coherent detection. Opt. Express **21**(9), 11585–11589 (2013). doi:10.1364/OE.21.011585

34. D.M. Kuchta, F.E. Doany, L. Schares, C. Neumeyr, A. Daly, B. Kögel, J. Rosskopf, M. Ortsiefer, Error-free 56 Gb/s NRZ modulation of a 1530 nm VCSEL link, in *2015 European Conference on Optical Communication (ECOC)*, 27 Sept 2015–1 Oct 2015, pp. 1–3. doi:10.1109/ECOC.2015.7341677
35. C. Xie, P. Dong, S. Randel, D. Pilori, P.J. Winzer, S. Spiga, B. Kögel, C. Neumeyr, M. Amann, Single-VCSEL 100-Gb/s short-reach system using discrete multi-tone modulation and direct detection, in *Optical Fiber Communication Conference*, Los Angeles, California, 22 Mar 2015. OSA Technical Digest (online) (Optical Society of America, 2015), p. Tu2H.2. doi:10.1364/OFC.2015.Tu2H.2
36. A. Vahdat, H. Liu, X. Zhao, C. Johnson, The emerging optical data center, in *Optical Fiber Communication Conference* (Optical Society of America, 2011), p. OTuH2
37. D. Apostolopoulos, P. Bakopoulos, D. Kalavrouziotis, G. Giannoulis, G. Kanakis, N. Iliadis, C. Spatharakis, J. Bauwelinck, H. Avramopoulos, Photonic integration enabling new multiplexing concepts in optical board-to-board and rack-to-rack interconnects, in *SPIE OPTO* (International Society for Optics and Photonics, 2014), pp. 89910D-89910D-89915
38. L.G. Kazovsky, W.-T. Shaw, D. Gutierrez, N. Cheng, S.-W. Wong, Next-generation optical access networks. J. Lightwave Technol. **25**(11), 3428–3442 (2007)
39. M.H. Eiselt, B.T. Teipen, Requirements for 100 Gb/s Metro Networks. Paper presented at the Optical Fiber Communication Conference and National Fiber Optic Engineers Conference, San Diego, California, 22 Mar 2009

http://www.springer.com/978-3-319-67001-0

Green Photonics and Electronics
Eisenstein, G.; Bimberg, D. (Eds.)
2017, XIV, 291 p. 164 illus., 118 illus. in color.,
Hardcover
ISBN: 978-3-319-67001-0